Journal of Geophysical Research: Space Physics

RESEARCH ARTICLE
10.1029/2018JA025406

Special Section:
Mars Aeronomy

Martian Electron Temperatures in the Subsolar Region: MAVEN Observations Compared to a One-Dimensional Model

W. K. Peterson[1], C. M. Fowler[1], L. A. Andersson[1], E. M. B. Thiemann[1], S. K. Jain[1], M. Mayyasi[2], T. M. Esman[3], R. Yelle[3], M. Benna[4], and J. Espley[4]

[1]LASP, University of Colorado Boulder, Boulder, CO, USA, [2]Center for Space Physics, Boston University, Boston, MA, USA, [3]Lunar and Planetary Laboratory, University of Arizona, Tucson, AZ, USA, [4]NASA/Goddard Space Flight Center, Greenbelt, MD, USA

Key Points:
- Densities and temperatures measured by MAVEN are used to evaluate electron heating and cooling terms in a 1-D energy equation
- MAVEN observations are consistent with the 1-D energy equation below ~210 km if the temperature is within the empirical bounds below 180 km
- The analysis suggests that electrons and neutrals reach thermal equilibrium below 120 km

Correspondence to:
W. K. Peterson,
bill.peterson@lasp.colorado.edu

Citation:
Peterson, W. K., Fowler, C. M., Andersson, L. A., Thiemann, E. M. B., Jain, S. K., Mayyasi, M., et al. (2018). Martian electron temperatures in the subsolar region: MAVEN observations compared to a one-dimensional model. *Journal of Geophysical Research: Space Physics*, *123*, 5960–5973. https://doi.org/10.1029/2018JA025406

Received 2 MAR 2018
Accepted 30 JUN 2018
Accepted article online 6 JUL 2018
Published online 27 JUL 2018

Abstract Prior to the Mars Atmospheric Volatile EvolutioN (MAVEN) mission, altitude profiles of the electron temperature in the Martian thermosphere were measured only twice. Because the rates of several geophysically important processes depend strongly on the electron temperature, models of the Martian thermosphere and atmospheric escape rates have not been well constrained. In this paper, we use densities and temperatures measured by MAVEN instruments and the one-dimensional model of Matta et al. (2014, https://doi.org/10.1016/j.icarus.2013.09.006) to test our understanding of the processes that determine the electron temperature. Our analysis is limited to inbound orbits where the magnetic field is within 30° of horizontal and the satellite is within 30° of the subsolar point at altitudes from 120 to 250 km. We introduce empirically adjusted electron temperatures below 180 km, where the MAVEN electron temperature measurements are known to be biased high. We introduce the concept of a local electron heating efficiency, which we define at a given altitude as the ratio of electron heating from photoionization to the total extreme ultraviolet energy deposited. Our analysis shows that MAVEN observations are consistent with the one-dimensional model below ~210 km if the electron heating efficiency varies with altitude, and the electron temperature is within the empirical bounds below 180 km we introduced. It indicates that above ~210 km electron heat conduction dominates extreme ultraviolet heating in determining electron temperature. Our analysis also suggests that in the subsolar region electrons and neutrals are in thermal equilibrium below 120 km.

1. Introduction

In planetary ionospheres, electron temperature is determined by a balance between heating, cooling, and heat transport and is sensitive to many local and remote drivers. The topic has been extensively investigated in the ionospheres of Earth, Venus, Mars, and some planetary moons (e.g., Schunk & Nagy, 2009). Until the arrival of the Mars Atmospheric Volatile EvoluntioN mission (MAVEN) at Mars in 2014, there were only two measured Martian electron temperature altitude profiles from the Viking landers above 200 km (Hanson et al., 1977). The rates of several geophysically important processes, such as the escape of energetic oxygen atoms produced by dissociative recombination of O_2^+, depend strongly on the plasma electron temperature (e.g., Andersson et al., 2010; Brecht et al., 2017; Ergun et al., 2016; Fox & Hac, 2009; Lillis et al., 2015, and others). Attempts to reconcile the Viking electron temperature profiles with models of the ionosphere required reasonable but unverified assumptions (e.g., Cui et al., 2015; Fallows et al., 2015a, 2015b; Fox & Yeager, 2006; Matta et al., 2014; Withers et al., 2014).

Recent progress has been made in understanding the Martian thermosphere and ionosphere with the advent of better estimates of the extreme ultraviolet (EUV) spectra incident on Mars and observations of Martian photoelectrons (e.g., Liemohn et al., 2003; Peterson et al., 2016; Sakai et al., 2015, 2016; Xu et al., 2015). The MAVEN data provide an opportunity to test our understanding of the relative importance of the various drivers of electron temperature in the Martian ionosphere.

Here we use measured values of densities and temperatures of thermospheric and ionospheric constituents in a one-dimensional formulation of the energy equation. Specifically, we follow the formulation used by Matta et al. (2014), which is shown as equation (1).

$$\frac{3}{2}N_e\ k\frac{\partial T_e}{\partial t} = Q_e - \Sigma L_e + \sin^2\alpha\frac{\partial}{\partial z}\left(\lambda_e\frac{\partial T_e}{\partial z}\right) - N_e\ k\ T_e\sin^2\alpha\frac{\partial V_e}{\partial z} - \frac{3}{2}N_e\ k\ V_e\sin^2\ \alpha\ \frac{\partial T_e}{\partial z} \quad (1)$$

Here N_e and T_e are the electron density and temperature, k is the Boltzmann constant; Q_e is the local electron heating from solar EUV radiation; ΣL_e is the sum of the five electron cooling terms described in Appendix A of Matta et al. (2014); α is the angle between the magnetic field direction and the horizontal, that is, the dip angle; Z is the local vertical direction; λ_e is the electron coefficient of thermal conductivity; and V_e is the electron velocity. We use the expression for λ_e given in Matta et al. The five terms on the right side of equation (1) represent local electron energy source and loss rates. Here we refer to them respectively as follows: electron heating, electron cooling, conduction, adiabatic expansion, and advection. This equation is valid under draped magnetic field conditions where the magnetic field is nearly parallel with the Martian surface.

Equation (1) states that the sum of energy source/loss rates at any altitude is proportional to the time derivative of the electron temperature at that altitude. All terms in the energy equation except the heating term depend on the local electron temperature. If there are no missing heating/cooling terms, and if the sum of the terms is zero within observational uncertainties at a given altitude, electrons are near thermal equilibrium there.

The purpose of this paper is to get a better understanding of the relative magnitudes of electron thermalization processes in the energy equation. MAVEN measurements are used to calculate the magnitude of the sum of the electron energy source/loss rates and its observational uncertainty as a function of altitude within 30° of the subsolar point on draped magnetic field lines at altitudes from 120 to 250 km. Values of the sum near zero indicate thermal equilibrium; values greater than the uncertainty of the sum indicate missing heating/cooling terms. As part of this analysis, we develop an empirical method to adjust for the systematic upward bias in MAVEN electron temperature measurements below ~750 K (Ergun et al., 2015) and estimate the uncertainty in the measured sum terms in the energy equation.

2. Data and Analysis

Data from three of the MAVEN instruments are presented: Electron temperature and density from the Langmuir Probe and Waves (LPW) instrument (Andersson et al., 2015), thermal ion and neutral densities and temperatures from the Neutral Gas and Ion Mass Spectrometer (NGIMS) instrument (Mahaffy et al., 2015), and daily total solar ionizing irradiance incident on Mars from the Extreme UltraViolet Monitor (EUVM) instrument (Eparvier et al., 2015). Data from the Magnetometer (MAG) instrument (Connerney et al., 2015) are used to select orbits for analysis.

We focus on data obtained from the inbound leg of the 218 orbits within 30°of the subsolar point from 120 to 250 km. These data were acquired in near northern spring equinoctial conditions in May 2015 and May 2017. During the 2015 interval, a MAVEN deep dip campaign sampled altitudes down to ~120 km (Ergun et al., 2015). During the 2017 interval periapsis was at ~160 km. All altitudes presented and discussed are with respect to the aeroid. The observed magnetic field was in a fully draped configuration (i.e., magnetic dip angle less than 30°in each of the 5-km sample bins) for the inbound portion below 300 km for 64 of these orbits. Data obtained under draped magnetic field conditions were obtained in 2015 on 25 orbits and in 2017 on 39 orbits. Figure 1 presents median electron temperature versus altitude in 5-km altitude bins for all 218 orbits considered in panel a. In panel b electron data for the subset of 64 orbits that the magnetic fields was in the draped configuration are displayed. For electron temperatures below ~750 K, the uncertainty in the LPW electron temperature fitting procedure becomes larger than the estimated temperature. Below this range the measured LPW temperatures are generally upper limits to the electron temperature (Ergun et al., 2015; Fowler et al., 2015). The temperature values near 550 K independent of altitude on some orbits between 150 and 180 km are features of the fitting procedures. The feature in the electron temperature around 150 km in Figure 1 is currently under investigation by the LPW team. It is unclear if this feature is real or an instrumental artifact. We note that the variability of the electron temperatures above 160 km is not significantly reduced under draped magnetic field conditions. Below 160 km the effect of draped magnetic fields on temperature variability is not clear because of limited data.

For each of the 64 subsolar, draped magnetic field configuration orbits we have assembled the density and temperature data presented in Figure 2. These data have been broken down into data acquired in May 2017 during low solar irradiance conditions in panels a and c and in May 2015 during more active solar conditions

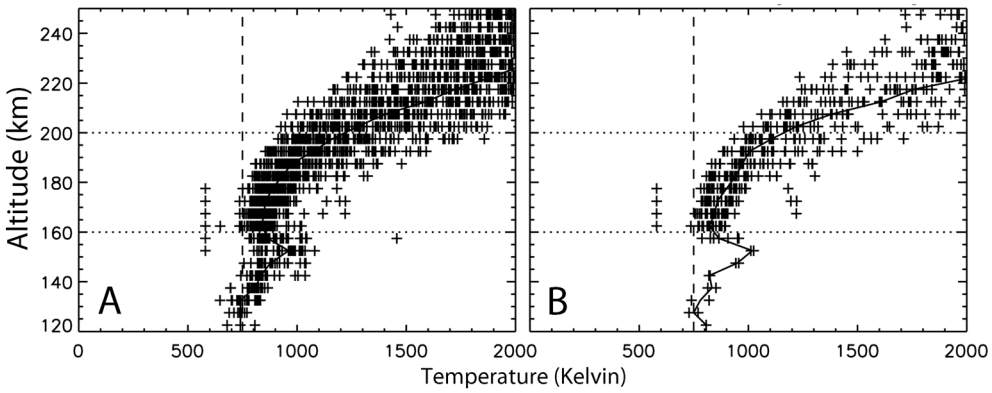

Figure 1. (a) Measured electron temperature versus altitude in 5-km altitude bins for the inbound portion of the 218 orbits within 30° of the subsolar point. (b) Electron temperature for the 64 inbound orbit portions where the average magnetic dip angle was less than 30° in each altitude bin. The median value in each altitude bin is indicated by the heavy solid line. The vertical dashed line at 750 K indicates the temperature where the uncertainty in the measured value is so large that the measured value becomes an upper limit to the temperature.

in panels b and d. The median solar irradiance at Mars in the 0- to 90-nm range is 34% higher in the 2015 interval, being 1.82×10^{-3} compared to 1.36×10^{-3} W/m^2 in the 2017 interval. Figures 2a and 2b show the electron temperature data shown in Figure 1 sorted into solar quiet (a) and active (b) intervals. The vertical lines in panels a and b below 190 km show the CO_2 temperatures derived from the CO_2 density profile below 190 km. Panels c and d present the electron, O, and CO_2 densities as indicated. Individual

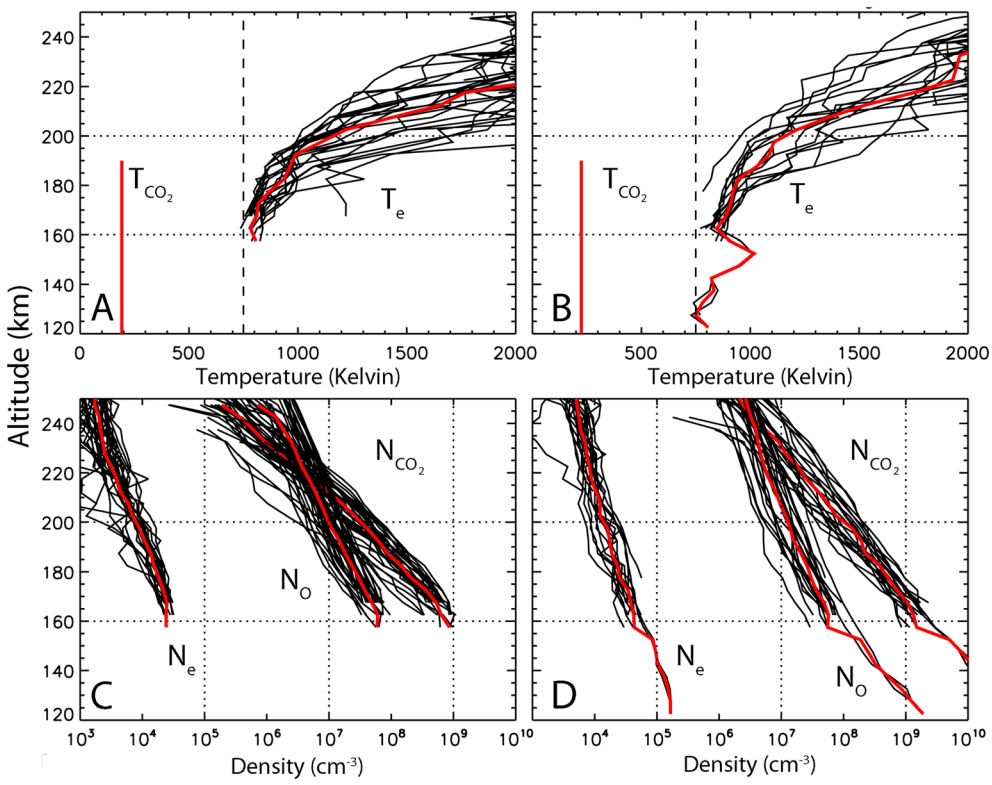

Figure 2. Densities and temperatures observed by MAVEN instruments in the subsolar region during solar quiet conditions (panels a and c) and solar active conditions (panels b and d). Electron and CO_2 temperatures are presented in panels (a) and (b). Electron, O, and CO_2 densities are presented in panels (c) and (d). Individual orbit data are shown as black lines. Median values are indicated by thicker red lines. Note that measured temperatures below 750 K are upper limits of the electron temperature. See text. MAVEN = Mars Atmospheric Volatile EvolutioN.

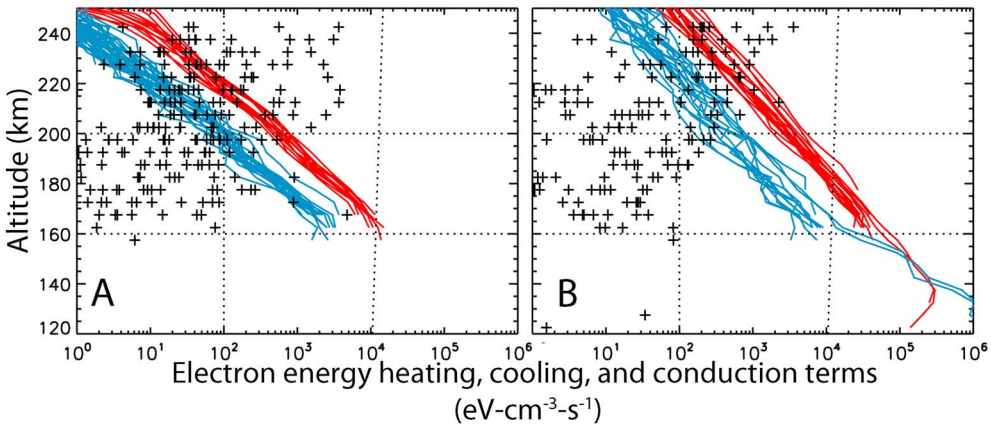

Figure 3. Upper limit of electron energy heating (red), cooling (blue), and conduction (black) terms in the energy equation (1) as a function of altitude derived from the data presented in Figure 2. The absolute values of the conduction term are displayed. Panel (a) presents data for solar quiet conditions, panel (b) for solar active conditions. Conduction values in panel (b) below 155 km are small and/or small and negative.

orbit data are shown as black lines. Median values are indicated by red lines. Note that the CO_2 temperatures are a median characteristic temperature below 190 km for the selected orbits, not a temperature profile. The median Mars Solar Orbit (MSO) latitude and solar zenith angles where the data in panels a and c were acquired are 21° and 38°; for panels b and d the median MSO latitude and solar zenith are 3° and 20°, respectively. In a typical deep dip pass below 200 km shown in panels b and d, MSO latitude and solar zenith angle varied by ~ 20°. For the data shown in panels a and c, MSO latitude and solar zenith angle varied by ~15° below 200 km.

We use MAVEN-measured quantities to calculate or estimate the magnitudes of the five terms in the energy equation as a function of altitude for the inbound segments of the 64 orbits meeting our criteria. Equation (1) applies locally. Calculation of local electron heating from photoionization (Q_e) directly from MAVEN measurements requires a model that calculates both the local total energy deposition rate (Q_T) and the rates of processes, such as neutral heating, air glow production, and energetic photoelectron production that do not contribute to local electron heating. The purpose of this paper is to test our understanding of the processes that determine the electron temperature, not to develop a new model for the Martian thermosphere. Our approach to estimating Q_e is to first calculate Q_T by using MAVEN EUVM solar EUV and NGIMS density data to produce a daily Chapman production function as a function of altitude for each 0.1-nm bin and integrating it from 0.5 to 90 nm as described in Thiemann et al. (2017). We use the cross sections given in Fox (1991). Q_T is an upper limit to Q_e. In the discussion section below we introduce *electron heating efficiency* to explore how varying the relative magnitude of Q_e/Q_T affects agreement between MAVEN data and the model.

Figure 3 shows the values of the first three terms: The upper limit of electron heating indicated by red, the negative electron cooling rate indicated by blue, and conduction indicated by the + symbols. Negative conduction rates are not shown. The total heating term in panel b maximizes at 6×10^5 at eV·cm^{-3}·s^{-1} at ~140 km. The second term in the energy equation (ΣL_e) is the sum of electron cooling resulting from electron scattering. Following Matta et al. (2014) we consider elastic collisions of electrons and CO_2, inelastic vibrational and rotational collisions of electrons and CO_2, inelastic fine structure interactions of electrons and atomic O, and elastic collisions with ions. To evaluate the cooling terms, we use the equations and electron thermal conductivity given in Appendix A of Matta et al. (2014). The sum of electron cooling from these processes is indicated by the blue lines in Figure 3. The sum of the cooling terms in panel b minimizes at -1×10^6 eV·cm^{-3}·s^{-1} at 120 km. The third term in the energy equation shown in Figure 3 as + symbols is conduction. This term depends on the product of the second derivative of temperature as a function altitude and the sine squared of the magnetic dip angle. The majority of conduction values are positive and shown in Figure 3. The temperature altitude profiles shown in Figures 2a and 2b are often nonlinear with altitude, which results in larger second derivatives as a function of altitude. The combination of relative small sine squared terms and larger second derivatives of T_e with altitude associated with rapid spatial and/or temporal variations of T_e results in the large variations in the conduction term.

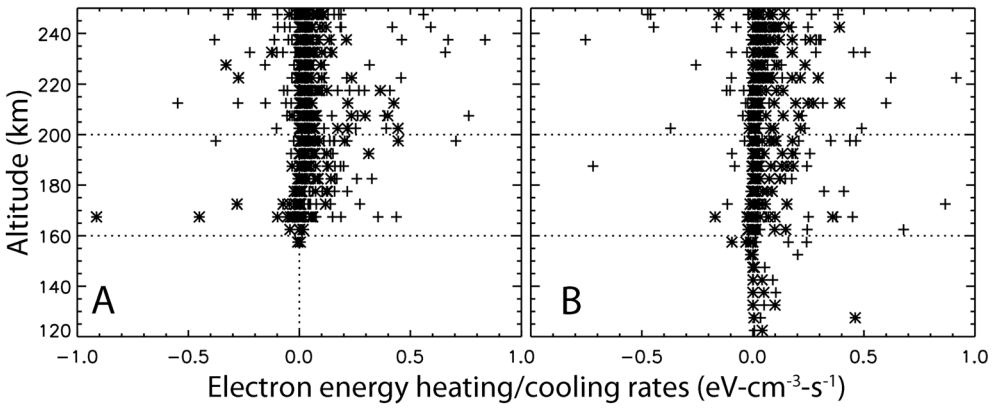

Figure 4. Adiabatic expansion (+) and advection (*) terms of the energy equation (1) as a function of altitude for lower (panel a) and higher (panel b) solar irradiance.

The fourth and fifth terms of the energy equation (1) are adiabatic expansion and advection, respectively. Both terms depend on the vertical electron velocity (V_e). Vertical electron velocity is approximately upward and perpendicular to the draped magnetic field in the orbits we selected. MAVEN instruments lack the sensitivity to determine V_e. However, a robust upper limit to V_e can be obtained by considering measurements of field-aligned currents (FAC). Brain and his colleagues (David Brain, private communication, 2017) have used magnetometer data from MAVEN and Mars Global Surveyor (MGS) to study FACs and their relation to Martian aurorae. They estimate that the MAVEN and MGS magnetometers are sensitive to FACs greater than 10^{-7} A/m^2. They have detected FAC only near regions with strong crustal fields, where the magnetic field is not in the draped configuration we are investigating. They have not detected FACs on draped magnetic field lines. Fillingim (2018), however, has observed horizontal (not vertical) FACs on draped magnetic field lines below 200 km on MAVEN with an intensity of ~10^{-6} A/m^2. If we assume an upward uniform current of 10^{-6} A/m^2 in the draped magnetic field region, we obtain an extreme upper limit of the electron upward velocity and therefore upper limits to the adiabatic expansion and advection terms. Upper limits to these terms are shown in Figure 4. The low values of the upper limits to the adiabatic expansion and advection terms shown in Figure 4, compared to the heating, predominant cooling, and conduction terms shown in Figure 3 demonstrate that adiabatic expansion and advection are not dominant drivers of electron temperature in the Martian subsolar ionosphere.

Figure 5 shows the sum of the five terms of the energy equation (1) as a function of altitude. This sum is proportional to the time derivative of T_e at each altitude. The sum comes from a large positive term (estimated upper limit of the heating rate), a large negative term (cooling), and the conduction term, which is variable.

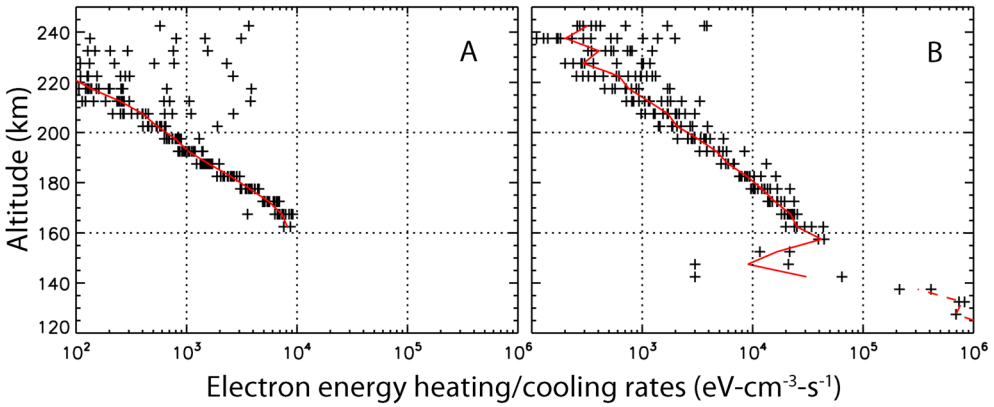

Figure 5. The sum of the terms on the right hand of the energy equation (1) as a function of altitude for lower (panel a) and higher (panel b) solar irradiance. Pluses indicate data from individual orbits. The thick red line is the median of values in each 5-km altitude bin. In panel (b) the net heating rate is negative below 140 km and is indicated by a dashed line.

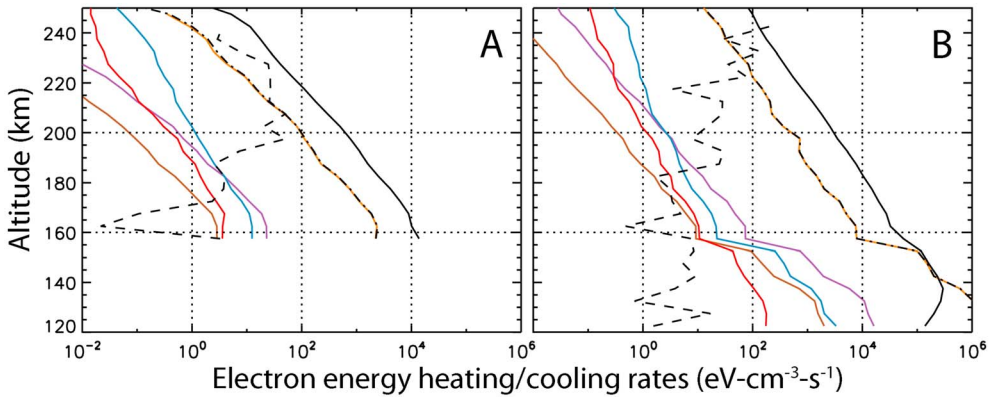

Figure 6. Absolute values of the median values of the upper limit of heating, conduction, and individual cooling terms in the energy equation (1) as a function of altitude for lower (panel a) and higher (panel b) solar irradiance. Key: black line = upper limit of heating; dashed black line = conduction; dash-dotted black line = sum of the five cooling terms considered here; orange line = cooling by inelastic collisions with CO_2 due to vibrational interactions; purple line = cooling by rotational interactions with CO_2; blue line = cooling by inelastic fine structure interactions with O; red line = cooling by elastic collisions with ions; and brown line = cooling by elastic collisions with CO_2. Note that the absolute values of the conduction term is presented.

Values less than the uncertainty in the sum indicate local thermal equilibrium. Before discussing the uncertainty in the values presented in Figure 5 we examine the components of the cooling term.

In the paragraphs below we use medians of the quantities shown in Figures 3–5. We defer discussion of the uncertainties associated with the deviation of measured values from the medians. We also address the known upward bias of measured electron temperatures less than 750 K below. Figure 6 shows the absolute values of the median values of the upper limit of heating (black line) and conduction (dashed black line) profiles from Figure 3. Also shown with colored lines are the components of the cooling term explained in the Appendix of Matta et al. (2014). Note that to evaluate the CO_2 vibrational cooling rates, we have used the formulation given in equation 43 of Dalgarno (1969) which differs from that given in equation A12 in Matta et al. The colored lines in Figure 6 display these subterms as a function of altitude. The dash-dotted black lines are the sum of the five cooling terms. The orange lines show cooling by inelastic collisions with CO_2 due to vibrational interactions. The purple lines give cooling by rotational interactions with CO_2. The blue lines show cooling by inelastic fine structure interactions with O. The red lines present cooling by elastic collisions with ions. Finally, the brown lines give cooling by elastic collisions with CO_2. The dominant cooling term is CO_2 vibrational cooling.

The cooling rates shown in Figure 6 depend on electron, ion, and neutral temperatures. We set the ion temperature to the average of the electron and neutral temperatures. Measured electron temperatures are upper limits below values of about 750 K (Andersson et al., 2015; Ergun et al., 2015; Fowler et al., 2015). This means that the cooling rates below ~180 km come from using upper limits of the electron temperature, rather than actual values of the electron temperature, which we know to be lower. In addition to adjusting the cooling rates by using more accurate temperatures, we also must consider the possibility that one or more of the cross sections used to calculate cooling could be incorrect. In particular, we consider the work of Campbell et al. (2008), who suggest, based on model/data comparisons of the Venusian thermosphere, larger cross sections of electron impact excitation of CO_2 vibrational modes. These larger cross sections increase the cooling rate of electrons interacting with CO_2 at the lowest temperatures.

There are several ways to estimate the electron temperature as a function of altitude where only upper limits to its value are available. The simplest is to scale linearly in altitude from 180 km where the MAVEN LPW temperature values are valid (i.e., >750 K) to the neutral temperature at the altitude where electrons are in thermal equilibrium with the neutrals. The altitude and temperature where thermal equilibrium is established is, however, uncertain. Bougher et al. (2015) report modeled and observed neutral temperature profiles to the lowest altitude (120 km) sampled by MAVEN. Their model profile is reproduced as the red line in Figure 7.

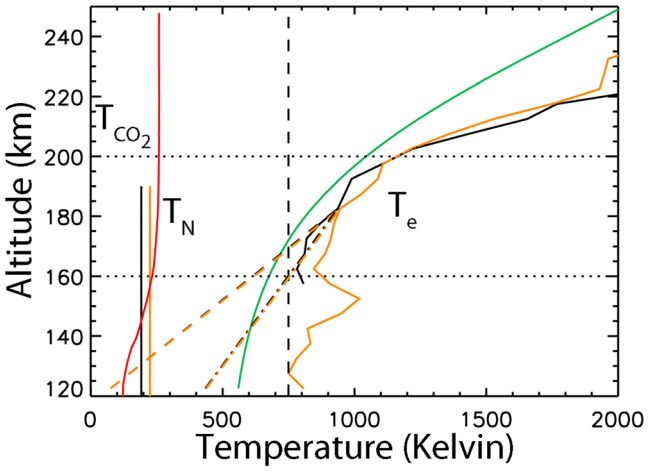

Figure 7. Neutral and electron temperatures. The vertical black line shows the observed median temperatures for $C0_2$ at the low solar irradiance intervals in May 2017; the vertical orange line shows the observed median CO_2 temperatures at high solar irradiance and lower altitudes in May 2015. The red line is the M-GITM neutral temperature profile that agreed well with observed argon temperatures reported by Bougher et al. (2015). The nonvertical solid black and orange lines show the electron temperatures measured by LPW for the low (black) and high (orange) solar irradiance intervals. The green line is the temperature profile given by Ergun et al. (2015). Below ~750 K, indicated by the dashed line, the electron temperatures measured by the MAVEN LPW instrument are upper limits. Our empirical extrapolations of the electron temperature below 180 km, which were introduced to bound the range of possible electron temperature profiles for the two intervals, are indicated by the dashed and dash-dotted lines. See text. MAVEN = Mars Atmospheric Volatile EvolutioN; LPW = Langmuir Probe and Waves.

To bound the range of possible low-altitude temperatures, we assumed two extreme temperature extrapolations. The first indicated by dashed lines scales linearly from an assumed thermal equilibrium of 75 K at 120 km to those measured by MAVEN/LPW at 180 km. The second method, indicated by the dash-dotted lines, scales from an assumed thermal equilibrium of 100 K at 80 km to the temperature measured by MAVEN/LPW at 180 km.

Ergun et al. (2015) have also reported an empirical fit to the temperature profiles obtained in the subsolar region during high solar irradiance conditions. These orbits include ones not meeting our draped magnetic field line conditions. The Ergun fit to measured temperatures is shown as a green line in Figure 7. It gives higher electron temperatures below 160 km than either of our empirical extrapolations.

Figure 8 presents temperature-adjusted cooling rates using the electron temperature profiles shown in Figure 7 where the solid and dashed colored lines correspond with the 120-km and 80-km temperature extrapolations, respectively. Only the dominant CO_2 vibrational cooling rates are shown. The orange lines are derived from the CO_2 vibrational cooling rates given in Dalgarno (1969). The green lines report cooling rates calculated using the Campbell et al. (2008) cross sections. Also shown are the unadjusted cooling rates (dotted green and orange lines), and an estimate of the upper limit of the electron heating term Q_e (solid black lines). For both intervals cooling is dominated by vibrational interactions between CO_2 and suprathermal electrons. The cooling rates calculated using the Campbell et al. (2008) cross sections are more sensitive to electron temperature variations. There are uncertainties associated with both the observed neutral and adjusted electron temperatures used to calculate the cooling rates seen in Figure 8. Uncertainties in the neutral temperature are a few tens of degrees kelvin. The uncertainty of several hundred degrees kelvin in the adjusted electron temperatures shown in Figure 7 below 160 km leads to the large range of possible cooling rates, that is, the range between the solid and dashed colored lines shown in Figure 8.

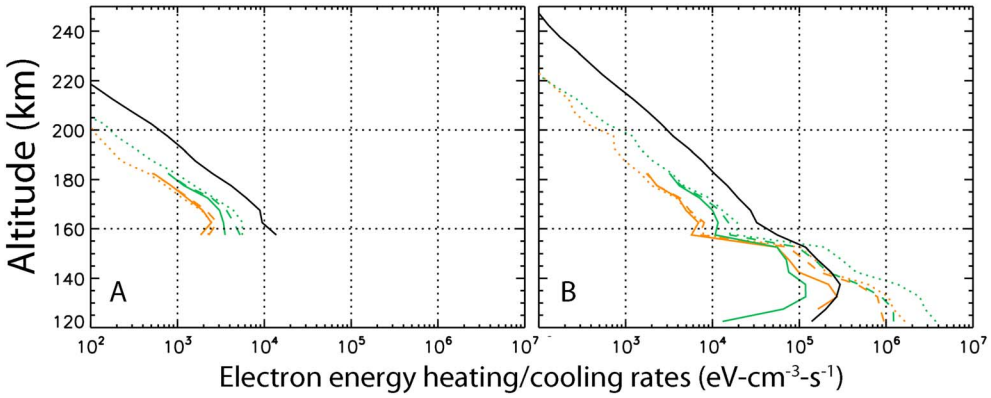

Figure 8. Temperature-adjusted values of the median values of the energy deposition and vibrational cooling rates as a function of altitude for lower (panel a) and higher (panel b) solar irradiance. Unadjusted cooling rates are shown as dotted lines. Temperature-adjusted values are shown below 180 km adjusted to 75 K at 120 km as solid lines and adjusted to 100 K at 80 km as dashed lines. The black solid line is the total EUV deposition rate (Q_T), which we are using as an upper limit on the local EUV electron heating rate. The orange lines are derived from vibrational cooling rates given in Matta et al. (2014). The green lines report cooling rates calculated using the Campbell et al. (2008) cross sections. EUV = ectreme ultraviolet.

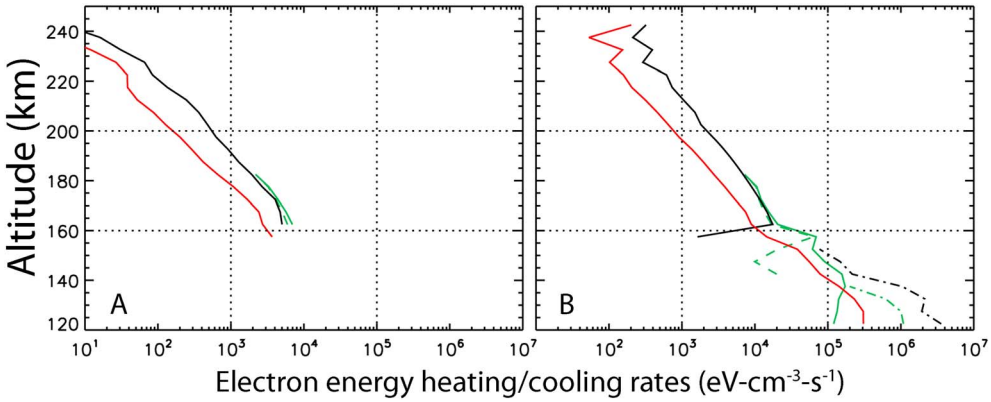

Figure 9. Net heating/cooling rates calculated with the T_e altitude profiles shown in Figure 7 and an estimate of their uncertainty. The sum of temperature-adjusted terms on the right hand of the energy equation (1) (black) as a function of altitude for lower solar irradiance (a) and higher solar irradiance (b). Positive values are shown as solid lines; negative values are shown as dash-dotted lines. The black lines are the median of the unadjusted sum of terms. The sum in this and following figures includes the Campbell et al. (2008) vibrational interaction terms. Solid green lines show the temperature extrapolation to 75 K at 120 km, which is positive at all altitudes displayed; dashed green lines show the temperature extrapolation to 100 K at 80 km, which is negative below 140 km as indicated by the green dash-dotted line. The red line shows estimates of the uncertainty of the sums presented. See text.

Figure 9 presents estimates of the sum of the median values of the five terms of the energy equation (1) as a function of altitude for temperature-adjusted cooling rates (green) and cooling rates calculated using measured electron temperatures (black). Solid lines indicate positive values; dash-dotted lines below ~155 km indicate negative values of the sum. Terms calculated using temperatures extrapolated to 75 K at 120 km are shown as solid lines; terms calculated using temperatures extrapolated to 100 K at 80 km are shown as dashed lines. The sum using the temperature extrapolation to 120 km is positive over the full altitude range; the sum using the extrapolation to 80 km is negative below 140 km as indicated by the green dash-dotted line. The electron heating rates used to produce Figure 9 are upper limits to electron heating (Q_T). The error in the sum of heating rates depends on both measurement error and uncertainties in the cross sections used. We estimate the error in the sums to be the square root of the sum of squares of 25% of the absolute magnitude of the upper limit of the heating, cooling, advection, and adiabatic expansion terms and 100% of the conduction term. The error estimate of the sum of terms is shown as a red line in Figure 9. Note that the sums in this and following figures include the Campbell et al. (2008) vibrational interaction terms. We have elected to use the Campbell et al. cross sections, because they are more consistent with the work of Morrison and Greene (1978).

Figure 9 shows that the net sum of heating and cooling terms above ~160 km is larger than its uncertainty for high (panel b) solar activity. Below this altitude the sum is a sensitive function of the electron temperature adjustment used. The adjustment that assumes thermal equilibrium with the neutrals at 120 km (solid green line in Figure 9) gives lower electron temperatures and lower cooling rates. The other extreme adjustment that assumes thermal equilibrium at 80 km (dashed green line in Figure 9) gives electron temperatures in the 400- to 550-K range between 120 and 140 km, higher cooling rates, and a negative net sum.

The heating term included in the sums shown in Figure 9 (Q_T) is the total energy deposited as a function of altitude. This includes energy that goes into heating neutrals, generating visible and UV emissions, production of energetic photoelectrons, and other process that do not contribute to local electron heating (Q_e). The purpose of this paper is to use MAVEN data to test our understanding of the relative importance of the various drivers of electron temperature in the Martian ionosphere, not to develop and implement a detailed model of how energy flows through the system and heats electrons. In section 1, we introduced "electron heating efficiency analogous to (neutral) heating efficiency used in many thermospheric models (e.g., Bougher et al., 2009 or Richards, 2012, and references therein). We defined electron heating efficiency as the percent of local energy deposited by EUV irradiance (Q_T) that results in local heating of electrons (Q_e). This efficiency factor is inherently a function of altitude.

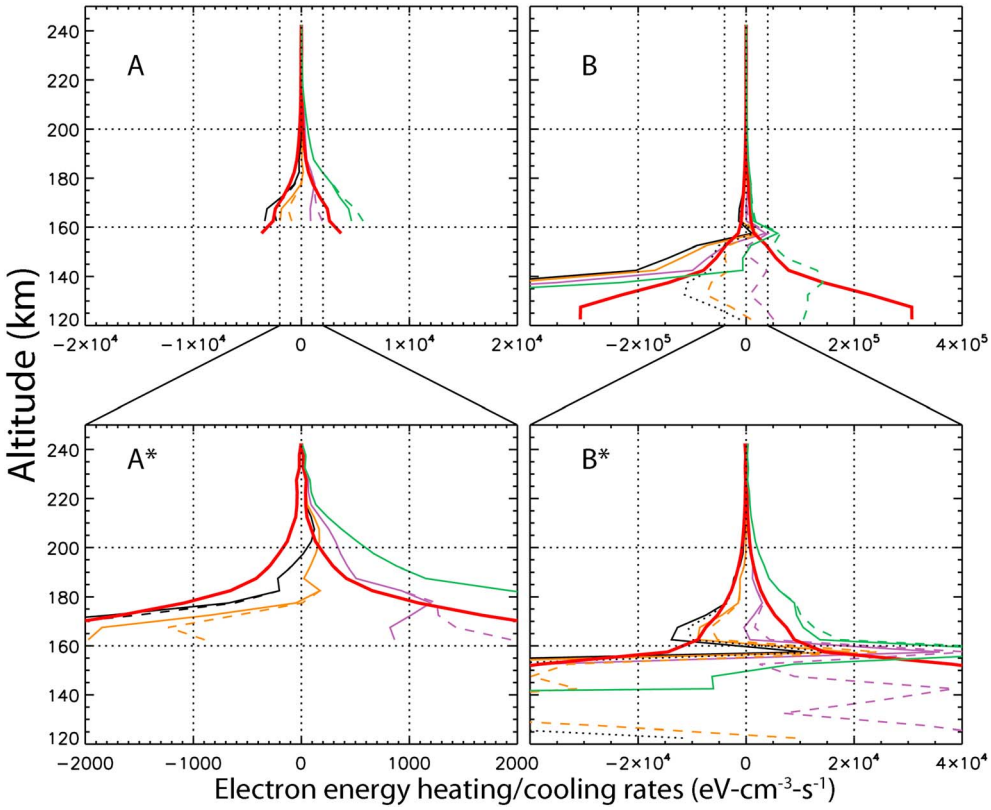

Figure 10. Net electron heating/cooling rates as a function of altitude under the assumption that 10%, 20%, 30%, or 90% (black, orange, purple, or green) of the total local heating rate shown in Figure 8 results in local electron heating. The top panels (a and b) cover the ranges from $\pm 2 \times 10^4$ and $\pm 4 \times 10^5$, respectively; the bottom panels (a* and b*) cover the ranges from $\pm 2 \times 10^3$ and $\pm 4 \times 10^4$. The thick red lines show estimates of the uncertainty of the sums presented. Data for low (high) solar activity are presented in panels a and a* (b and b*). The data in panels a and b are reproduced with a smaller range of the abscissa in panels a* and b*. Solid lines indicate cooling rates calculated assuming electron/neutral temperature equilibrium at 120 km at 75 K. Dashed lines show results assuming electron temperature equilibrium at 80 km at 100 K.

Figure 10 presents on two linear scales the net heat/cooling rate using electron heating efficiencies of 10% (black), 20% (orange), 30% (purple), and green (90%) using the Campbell et al. (2008) vibrational cooling rates for the two intervals under consideration. The top panels (a and b) cover the ranges from $\pm 2 \times 10^4$ to $\pm 4 \times 10^5$, respectively; the bottom panels (a* and b*) cover the ranges from $\pm 2 \times 10^3$ to $\pm 4 \times 104$. Data are shown for the two temperature adjustments of cooling rates given in Figure 8. Solid lines indicate cooling rates calculated assuming electron/neutral temperature equilibrium at 120 km at 75 K. Dashed lines assume electron/neutral temperature equilibrium at 80 km at 100 K.

The net electron heating/cooling rates at any altitude are proportional to the time derivative of the electron temperature at that altitude. Values of the sum that are within the limits of uncertainty (i.e., red lines in Figure 10) are consistent with electron thermal equilibrium. Although not visible in Figure 10, even the 10% local electron heating efficiency assumption results in sums that are greater than the estimated uncertainty above ~200 km. This and other features in Figure 10 are discussed below.

3. Discussion

MAVEN measurements of electron temperature and calculated local energy source/loss rates in the Martian subsolar ionosphere in the framework of the one-dimensional model of Matta et al. (2014) have been presented above. MAVEN data were acquired in subsolar regions where the magnitude of the latitude and longitude in MSO coordinates are less than 30° and the magnetic field is in a draped configuration (i.e., the direction of the local magnetic field is within 30° of horizontal below 300 km for the inbound portion of each orbit).

The energy equation (1) relates the time derivative of the electron temperature to the sum of local energy source/loss rates. Because electrons have high collision rates below 250 km, they equilibrate to local conditions on time scales much shorter than the ~10 min required to obtain an altitude profile on an inbound MAVEN orbit. All terms in the energy equation except the heating term depend on the local electron temperature, so if the sum of the terms is near zero within observational uncertainties at a given altitude, electrons are near thermal equilibrium there.

Ergun et al. (2015) show that the electron temperatures measured by the MAVEN LPW instrument and presented in Figure 2 are generally valid for values greater than ~750 K. They are systematically biased to yield a higher measurement of T_e than the actual value for a temperatures below this threshold detection value. We introduced an empirical method to adjust the measured T_e to more accurately reflect the actual electron temperatures below 180 km. Specifically, linear extrapolations of the electron temperature at 180 km to an estimate of the neutral temperature at an estimated altitude where the electron and neutral temperatures are equal are used. We choose the two end points of the extrapolation to bound the range of possibilities: 75 K at 120 km and 100 K at 80 km. The measured and empirically adjusted electron temperature profiles are presented in Figure 7. The Ergun et al. (2015) fit to the measured temperature profile also shown in Figure 7 gives higher temperatures below 160 km than either of our empirical adjustments.

The dominant vibrational electron-CO_2 cooling rates presented in Figure 8 were calculated using measured densities and temperatures and two independently determined cross sections. The values given by orange lines were calculated using the equation 43 in Dalgarno (1969). The values presented as green lines were calculated using the Campbell et al. (2008) cross sections. Campbell et al. used these larger cross sections to explain Venusian electron temperatures. Campbell and his colleagues suggested that the cross sections should also be applied to the Martian ionosphere. Above 180 km, where the temperatures are not adjusted, the Campbell cross sections give systematically larger cooling rates. Below 180 km we consider a range of adjusted temperatures. Below 160 km the range of adjusted cooling rates calculated using the Campbell cross sections is larger and includes the range calculated using the Dalgarno cross sections. We have elected to use the Campbell et al. cross sections in the analysis below because Campbell et al. show that they are more consistent with the work of Morrison and Greene (1978).

The upper limit to the heating rates (Q_T) presented in Figure 8 and used in calculating the net sum of heating and cooling rates displayed in Figures 9 show that the sum of the heating and cooling rates, even when adjusted electron temperatures are used, is greater than or equal to the error estimate for altitudes above 140 km under both conditions of solar irradiance considered. It is necessary, therefore, to consider the partition of deposited energy into processes that do and do not locally heat electrons. Rather than develop and implement a new photochemical model that includes photoelectron energy transport, we introduced the concept of local electron heating efficiency. We defined electron heating efficiency as the percent of local energy deposited by EUV irradiance (Q_T) that results in local heating of electrons (Q_e in equation (1)). Richards (2012) estimated that, on Earth, half of the locally deposited EUV photon energy goes into the translational energy of photoelectrons and most of the other half goes into the potential energy of ions, which drives the local photochemistry. The model developed by Jain and Bhardwaj (2011) shows that ~10% of the solar EUV irradiance goes directly into visible and UV emissions and that this fraction is relatively constant with altitude. EUV irradiance also provides energy to neutrals, ions, and photoelectrons. It also provides chemical energy that can lead directly to ion or neutral escape (e.g., Lillis et al., 2017; Richards, 2012), and not contribute to local heating of electrons. Energetic photoelectrons can deposit their energy either locally, when their mean free paths are short, or nonlocally, when their mean free paths are long.

Figure 10 demonstrates that the net heating/cooling rates between ~140 and ~210 km calculated using MAVEN data are generally within their estimated uncertainties for electron heating efficiencies between 10% and 30%. In the rest of this section we discuss the relative importance of terms in the energy equation in the altitude region between ~140 and ~210 km, above 210 km, and below 140 km.

3.1. Altitudes Between 140 and 210 km

The comparison of model, observations, and observational uncertainties between ~140 and ~210 indicates that equation (1) evaluated with temperature-adjusted MAVEN data and the electron-CO_2 vibrational excitation interaction parameterized by Campbell et al. (2008) is consistent with electron thermal equilibrium in this

altitude range. We do not have to introduce other sources or sinks of energy or systematic errors in the cross sections used to calculate the heating and cooling rates to get model/data consistency. The relatively large uncertainty of the values shown in Figure 10, however, do not allow us to determine if the electron-$C0_2$ vibrational excitation interaction parameterized by Campbell et al. (2008) is better than that used by Dalgarno (1969).

The empirical electron heating efficiency factor shown in Figure 10 appears to depend on solar activity as well as altitude. Low solar activity (panel a) suggests a factor less than 10%, whereas high solar activity suggests a factor of ~20%. The large uncertainties in the sum of the terms in the energy equation do not allow us to confirm this suggestion, however.

Regarding photoelectron energy transport: most energetic photoelectrons depositing energy in the subsolar region are produced there. In the subsolar region below 200 km and in the draped magnetic field configuration we are investigating, photoelectron energy deposition is essentially a local process. Peterson et al. (2016) and others have shown that most of the photoelectron energy is carried by photoelectrons with energies less than 100 eV. Below 200 km the electron gyro radius for electrons with energy less than 100 eV is on average less than 1.5 km. In the draped magnetic field geometry and 5-km altitude bins under consideration this means that vertical transport of energy by photoelectrons is negligible.

Photoelectrons carry energy parallel to the draped magnetic fields and deposit it away from their production point. The characteristic distance for parallel energy transfer is their mean free path, which depends on energy, neutral density, and total cross sections. We determined that for the average low solar activity conditions and magnetic configurations below 200 km investigated the mean free paths for 1, 20, and 100 eV photoelectrons are less than 200, 800, and 2,000 km, respectively. For the densities encountered in the average high solar activity conditions investigated, the mean free paths are at least half those values. We are comparing data acquired in the subsolar region within 30° or ~1,700 km of the subsolar point. Most photoelectrons produced in this region will therefore deposit their energy within it. More important most energetic photoelectrons depositing energy in the subsolar region as we define it are produced there.

3.2. Altitudes Above 210 km

Figure 3 shows that above 210 km the conduction term, $\sin^2\alpha\frac{\partial}{\partial z}\left(\lambda e\frac{\partial T_e}{\partial z}\right)$, is comparable in magnitude to, and has more variability than, the other terms in the energy equation. The conduction term depends primarily on the second derivative of the electron temperature with altitude (z). The magnetic dip angle (α) is less than 30° for the data presented here, and the electron coefficient of thermal conductivity (λe) increases monotonically with altitude. Subsolar electron temperature altitude profiles, however, are seldom monotonic. Ergun et al. (2015), Fowler et al. (2015), Sakai et al. (2016), and Figure 2 show altitude profiles of electron temperature above 200 km, which do not have a monotonic increase of temperature with altitude, but rather increasing and decreasing rates of temperature with altitude. These normally occurring changes in electron temperature with altitude give rise to large and variable values of the second derivative of temperature with altitude and consequently to the magnitude of the conduction term. It is not possible to determine the relative magnitudes of the spatial and temporal components of the observed electron temperature variations. The estimate of total uncertainty in the sum of terms in the energy equation shown in Figures 9 and 10 includes an estimate of 100% uncertainty in the median value of the conduction term. The analysis above shows that the conduction term dominates the sum of the terms in the energy equation above 210 km altitude. The data above 210 km also suggest that there are energy sources (heating terms) at high altitudes and/or upstream or downstream of the sample locations that are not included in the energy equation we are using.

Ergun et al. (2006) suggested that ionospheric electrons could be directly heated by electric field power generated in the solar wind that propagates into the ionosphere. Fowler et al. (2017) show that below about 200 km, heating by this mechanism is negligible. At higher altitudes, wave heating, a term not included in the energy equation used here, would increase the electron temperature. Sakai et al. (2016), however, found that higher than expected electron temperatures in 300-km altitude range could be reproduced using specific subsolar magnetic field configurations.

We find that, above 210 km in the subsolar region, electron heat conduction is the dominant term in the one-dimensional heat equation considered. The analysis is also consistent with plasma wave heating and magnetic configuration effects significantly contributing to determining electron temperature above 210 km.

The observations presented here, however, do not have adequate time or altitude resolution to determine the relative magnitudes of these processes.

3.3. Altitudes Below 140 km

Figure 3 shows that the maximum rate of EUV energy input occurs below ~140 km and that cooling rates continue to increase below this altitude. This is consistent with the altitude of peak electron density (124 km) derived by Ergun et al. (2015) from 28 subsolar orbits including both those from the draped magnetic field conditions investigated here as well as magnetic field configurations modified by Martian crustal fields. It is also consistent with the EUV absorption estimates of 135 km for the same orbits made by Mendillo et al. (2017).

Below the altitude of peak EUV energy deposition the neutral density becomes so large that even the most energetic photoelectrons deposit their energy locally. Since ~10% of the EUV energy goes directly into visible and UV emissions (e.g., Jain & Bhardwaj, 2011), the maximum possible heating efficiency is ~90%. Figure 8b shows that below 200 km cooling rates depend strongly on electron temperature. Temperature-adjusted cooling rates that assume electron-neutral thermal equilibrium at 120 km and a 90% heating efficiency (solid green line) give a sum of the terms in the energy equation near or below the lower limit of the uncertainty in the sum. Whereas, the significantly larger temperature-adjusted cooling rates assuming electron-neutral thermal equilibrium at 80 km (dashed green lines) give a sum of terms in the energy equation less than the upper limit of the uncertainty below ~140 km. This is consistent with the two assumed adjusted temperature profiles shown in Figure 7 bounding the range of actual temperature profiles. This result suggests

1. that the altitude where electrons and neutrals are in thermal equilibrium lies below 120 km;
2. that the electron temperature profile given by Ergun et al. (2015) shown by the green line in Figure 7 overestimates the electron temperature below ~150 km.

It is important to note that all of the data obtained below 140 km are obtained near periapsis. Here the separation of vertical and horizontal variations in plasma parameters is difficult and the empirically adjusted electron temperatures used in the calculation are all below 750 K and as such may be biased. The limited data available to date below 140 km in the subsolar region, therefore, preclude a more detailed examination of variations in peak EUV energy deposition, electron temperature, and peak electron density.

3.4. Other Considerations

Jakosky et al. (2017) reported that in May 2015 the Martian homopause was between 110 and 140 km and the exobase between 180 and 190 km. Later in the mission when the solar irradiance was lower the exobase was as low as 150 km. (The homopause is the altitude below which the neutral atmosphere is characterized by one scale height; the exobase is the altitude where neutral particles transition from a collision dominated to a transport-dominated environment). No features in the electron temperature or the local electron heating or cooling rates were found associated with the Martian homopause or exobase.

4. Conclusions

We used electron temperatures and densities measured on the MAVEN spacecraft during two intervals where the subsolar Martian ionosphere was sampled on draped magnetic field lines below 250 km to examine the relative importance of terms in the electron energy equation. As part of our analysis we introduced methods to empirically adjust electron temperatures below 750 K where temperatures measured by the LPW instrument are upper limits to the real electron temperature. We introduced and used the concept of electron heating efficiency to probe the MAVEN data and our simple one-dimensional model.

The analysis shows the following:

- The observationally based electron heating efficiency tool we introduced is not precise: multiple values are consistent with the data and empirical bounds on electron temperatures we introduced in Figure 7.
- MAVEN observations are consistent with the one-dimensional model below 210 km if the electron heating efficiency varies with altitude and solar activity. Above 210 km electron heat conduction appears to be the dominant processes determining electron temperature.
- Electron heat conduction rates are determined by spatial and/or temporal variations in the electron temperature in our one-dimensional formulation.

- The adiabatic expansion and advection terms in the energy equation are negligible at all altitudes investigated.
- The CO_2 electron vibrational excitation cross sections reported by Campbell et al. (2008) as well as those reported by Dalgarno (1969) are both consistent with MAVEN observations.
- MAVEN data and our empirical adjustments to electron temperature suggest that the altitude where electrons and neutrals are in thermal equilibrium lies below 120 km.
- It is possible that other sources or sinks of energy such as wave heating above 200 km have magnitudes comparable to those we have considered, but the data lacks the resolution to demonstrate that they are important.

The MAVEN data and model comparison presented here show that it is now possible to make progress understanding electron thermalization processes in the Martian thermosphere. The next steps are to evaluate rather than estimate electron heating efficiency as a function of altitude, and to extend analysis to regions closer to the terminator where photoelectron transport is significant.

Acknowledgments
W. K. P. thanks Phil Richards and Allan Burns for helpful comments. We thank the many hundreds of people who made the MAVEN project successful. This work was sponsored by NASA through the Mars Exploration Program. MAVEN data are available on NASA's Planetary Data System.

References

Andersson, L., Ergun, R. E., Delory, G. T., Eriksson, A., Westfall, J., Reed, H., et al. (2015). The Langmuir probe and waves (LPW) instrument for MAVEN. *Space Science Reviews*, *195*(1-4), 173–198. https://doi.org/10.1007/s11214-015-0194-3

Andersson, L., Ergun, R. E., & Stewart, A. I. F. (2010). The combined atmospheric photochemistry and ion tracing code: Reproducing the Viking lander results and initial outflow results. *Icarus*, *206*(1), 120–129. https://doi.org/10.1016/j.icarus.2009.07.009

Bougher, S., Jakosky, B., Halekas, J., Grebowsky, J., Luhmann, J., Mahaffy, P., et al. (2015). MAVEN Deep Dip campaign reveals thermosphere and ionosphere variability. *Science*, *350*(6261), aad0459. https://doi.org/10.1126/science.aad0459

Bougher, S. W., McDunn, T. M., Zoldak, K. A., & Forbes, J. M. (2009). Solar cycle variability of Mars dayside exospheric temperatures: Model evaluation of underlying thermal balances. *Geophysical Research Letters*, *36*, L05201. https://doi.org/10.1029/2008GL036376

Brecht, S. H., Ledvina, S. A., & Jakosky, B. M. (2017). The role of the electron temperature on ion loss from Mars. *Journal of Geophysical Research: Space Physics*, *122*, 8375–8390. https://doi.org/10.1002/2016JA023510

Campbell, L., Brunger, M. J., & Rescigno, T. N. (2008). Carbon dioxide electron cooling rates in the atmospheres of Mars and Venus. *Journal of Geophysical Research*, *113*, E08008. https://doi.org/10.1029/2008JE003099

Connerney, J. E. P., Espley, J., Lawton, P., Murphy, S., Odom, J., Oliversen, R., & Sheppard, D. (2015). The MAVEN magnetic field investigation. *Space Science Reviews*, *195*(1-4), 257–291. https://doi.org/10.1007/s11214-015-0169-4

Cui, J., Galand, M., Zhang, S. J., Vigren, E., & Zou, H. (2015). The electron thermal structure in the dayside Martian ionosphere implied by the MGS radio occultation data. *Journal of Geophysical Research: Planets*, *120*, 278–286. https://doi.org/10.1002/2014JE004726

Dalgarno, A. (1969). Inelastic collisions at low energies. *Canadian Journal of Chemistry*, *47*(10), 1723–1729. https://doi.org/10.1139/v69-284

Eparvier, F. G., Chamberlin, P. C., Woods, T. N., & Thiemann, E. M. B. (2015). The solar extreme ultraviolet monitor for MAVEN. *Space Science Reviews*, *195*(1-4), 293–301. https://doi.org/10.1007/s11214-015-0195-2

Ergun, R., Andersson, L., Peterson, W., Brain, D., Delory, G., Mitchell, D., et al. (2006). Role of plasma waves in Mars' atmospheric loss. *Geophysical Research Letters*, *33*, L14103. https://doi.org/10.1029/2006GL025785

Ergun, R. E., Andersson, L. A., Fowler, C. M., Woodson, A. K., Weber, T. D., Delory, G. T., et al. (2016). Enhanced O_2^+ loss at Mars due to an ambipolar electric field from electron heating. *Journal of Geophysical Research: Space Physics*, *121*, 4668–4678. https://doi.org/10.1002/2016JA022349

Ergun, R. E., Morooka, M. W., Andersson, L. A., Fowler, C. M., Delory, G. T., Andrews, D. J., et al. (2015). Dayside electron temperature and density profiles at Mars: First results from the MAVEN Langmuir probe and waves instrument. *Geophysical Research Letters*, *42*, 8846–8853. https://doi.org/10.1002/2015GL065280

Fallows, K., Withers, P., & Matta, M. (2015a). An observational study of the influence of solar zenith angle on properties of the M1 layer of the Mars ionosphere. *Journal of Geophysical Research: Space Physics*, *120*, 1299–1310. https://doi.org/10.1002/2014JA020750

Fallows, K., Withers, P., & Matta, M. (2015b). Numerical simulations of the influence of solar zenith angle on properties of the M1 layer of the Mars ionosphere. *Journal of Geophysical Research: Space Physics*, *120*, 6707–6721. https://doi.org/10.1002/2014JA020947

Fillingim, M. (2018). Ionospheric currents at Mars and their electrodynamic fields, in Electric Currents in Geospace and Beyond, Geophysical Monograph 235, edited by Andreas Keiling, Octav Marghitu, and Michael Wheatland, © 2018 American Geophysical Union. Published 2018 by john Wiley & sons, Inc.

Fowler, C. M., Andersson, L., Ergun, R. E., Morooka, M., Delory, G., Andrews, D. J., et al. (2015). The first in situ electron temperature and density measurements of the Martian nightside ionosphere. *Geophysical Research Letters*, *42*, 8854–8861. https://doi.org/10.1002/2015GL065267

Fowler, C. M., Ergun, R. E., Andersson, L., Peterson, W. K., Hara, T., Mcfadden, J., et al. (2017). Ion heating in the Martian ionosphere. *Journal of Geophysical Research: Space Physics*, *122*, 10,612–10,625. https://doi.org/10.1002/2017JA024578

Fox, J. L. (1991). Cross sections and reaction rates of relevance to aeronomy, U. S. Natl. Rep. Int. Union Geod. Geophys. 1987–1990. *Reviews of Geophysics*, *29*, 1110.

Fox, J. L., & Hac, A. B. (2009). Photochemical escape of oxygen from Mars: A comparison of the exobase approximation to a Monte Carlo method. *Icarus*, *204*(2), 527–544. https://doi.org/10.1016/j.icarus.2009.07.005

Fox, J. L., & Yeager, K. E. (2006). Morphology of the near-terminator Martian ionosphere: A comparison of models and data. *Journal of Geophysical Research*, *111*, A10309. https://doi.org/10.1029/2006JA011697

Hanson, W. B., Sanatani, S., & Zuccaro, D. R. (1977). The Martian ionosphere as observed by the Viking retarding potential analyzers. *Journal of Geophysical Research*, *82*(28), 4351–4363. https://doi.org/10.1029/JS082i028p04351

Jain, S. K., & Bhardwaj, A. (2011). Model calculation of N_2 Vegard-Kaplan band emissions in Martian dayglow. *Journal of Geophysical Research*, *116*, E07005. https://doi.org/10.1029/2010JE003778

Jakosky, B. M., Slipski, M., Benna, M., Mahaffy, P., Elrod, M., Yelle, R., et al. (2017). Mars' atmospheric history derived from upper-atmosphere measurements of $^{38}Ar/^{36}Ar$. *Science*, *355*(6332), 1408–1410. https://doi.org/10.1126/science.aai7721

Liemohn, M. W., Mitchell, D. L., Nagy, A. F., Fox, J. L., Reimer, T. W., & Ma, Y. (2003). Comparisons of electron fluxes measured in the crustal fields at Mars by the MGS magnetometer/electron reflectometer instrument with a B field-dependent transport code. *Journal of Geophysical Research*, *108*(E12), 5134. https://doi.org/10.1029/2003JE002158

Lillis, R. J., Brain, D. A., Bougher, S. W., Leblanc, F., Luhmann, J. G., Jakosky, B. M., et al. (2015). Characterizing atmospheric escape from Mars today and through time, with MAVEN. *Space Science Reviews*, *195*(1–4), 357–422. https://doi.org/10.1007/s11214-015-0165-8

Lillis, R. J., Deighan, J., Fox, J. L., Bougher, S. W., Lee, Y., Combi, M. R., et al. (2017). Photochemical escape of oxygen from Mars: First results from MAVEN in situ data. *Journal of Geophysical Research: Space Physics*, *122*, 3815–3836. https://doi.org/10.1002/2016JA023525

Mahaffy, P., Benna, M., King, T., Harpold, D. N., Arvey, R., Barciniak, M., et al. (2015). The neutral gas and ion mass spectrometer on the Mars Atmosphere and Volatile Evolution Mission. *Space Science Reviews*, *195*(1-4), 49–73. https://doi.org/10.1007/s11214-014-0091-1

Matta, M., Galand, M., Moore, L., Mendillo, M., & Withers, P. (2014). Numerical simulations of ion and electron temperatures in the ionosphere of Mars: Multiple ions and diurnal variations. *Icarus*, *227*, 78–88. https://doi.org/10.1016/j.icarus.2013.09.006

Mendillo, M., Narvaez, C., Vogt, M. F., Mayyasi, M., Forbes, J., Galand, M., et al. (2017). Sources of ionospheric variability at Mars. *Journal of Geophysical Research: Space Physics*, *122*, 9670–9684. https://doi.org/10.1002/2017JA024366

Morrison, M. A., & Greene, A. E. (1978). Electron cooling by excitation of carbon dioxide. *Journal of Geophysical Research*, *83*(A3), 1172–1174. https://doi.org/10.1029/JA083iA03p01172

Peterson, W. K., Thiemann, E. M. B., Eparvier, F. G., Andersson, L., Fowler, C. M., Larson, D., et al. (2016). Photoelectrons and solar ionizing radiation at Mars: Predictions versus MAVEN observations. *Journal of Geophysical Research: Space Physics*, *121*, 8859–8870. https://doi.org/10.1002/2016JA022677

Richards, P. G. (2012). Re-evaluation of thermosphere heating by solar EUV and UV radiation. *Canadian Journal of Physics*, *90*, 1. https://doi.org/10.1139/p11-109

Sakai, S., Andersson, L., Cravens, T. E., Mitchell, D. L., Mazelle, C., Rahmati, A., et al. (2016). Electron energetics in the Martian dayside ionosphere: Model comparisons with MAVEN data. *Journal of Geophysical Research: Space Physics*, *121*, 7049–7066. https://doi.org/10.1002/2016JA022782

Sakai, S., Rahmati, A., Mitchell, D. L., Cravens, T. E., Bougher, S. W., Mazelle, C., et al. (2015). Model insights into energetic photoelectrons measured at Mars by MAVEN. *Geophysical Research Letters*, *42*. https://doi.org/10.1002/2015GL065169

Schunk, R., & Nagy, A. (2009). *Ionospheres: Physics, plasma physics, and chemistry*. Cambridge, UK: Cambridge University Press.

Thiemann, E. M. B., Chamberlin, P. C., Eparvier, F. G., Templeman, B., Woods, T. N., Bougher, S. W., & Jakosky, B. M. (2017). The MAVEN EUVM model of solar spectral irradiance variability at Mars: Algorithms and results. *Journal of Geophysical Research: Space Physics*, *122*, 2748–2767. https://doi.org/10.1002/2016JA023512

Withers, P., Fallows, K., & Matta, M. (2014). Predictions of electron temperatures in the Mars ionosphere and their effects on electron densities. *Geophysical Research Letters*, *41*, 2681–2686. https://doi.org/10.1002/2014GL059683

Xu, S., Liemohn, M. W., Peterson, W. K., Fontenla, J., & Chamberlin, P. (2015). Comparison of different solar irradiance models for the superthermal electron transport model for Mars. *Planetary and Space Science*, *119*, 62–68. https://doi.org/10.1016/j.pss.2015.09.008